Journal of Materials Chemistry C

ROYAL SOCIETY OF CHEMISTRY

PAPER

View Article Online
View Journal | View Issue

Cite this: J. Mater. Chem. C, 2023, 11, 5461

Dynamic CPL switching realized in chiral Mn-based metal halides with reversible thermochromism†

Tianyong Zhang,‡[ab] Huimin Kang,‡[a] Bin Li,[ab] Jin Zhou,[c] Peisheng Zhao,[a] Tianzhe Zhao,[a] Xiaolei Li[a] and Shuang Jiang *[ab]

Received 15th December 2022,
Accepted 22nd March 2023

DOI: 10.1039/d2tc05349g

rsc.li/materials-c

Circularly polarized luminescence (CPL) active materials have attracted much attention due to their extensive applications in 3D optical displays and encrypted transmission. The switchable regulation of CPL is of great importance for applications such as spintronics. However, the study of intelligent regulation is scarce, especially the simultaneous regulation of the color and direction of polarization. In this paper, we have successfully prepared switchable CPL active Mn-based metal halides $(R\text{-}/S\text{-Br-MBA})_3MnBr_5$, whose single crystal displays orange CPL at 634 nm at room temperature. With the increase of temperature, the CPL displayed by single crystals gradually turns into green at 520 nm and the CPL signal flips, variable emission color and CPL switch in +/− are achieved in the prepared chiral manganese halides. This emission switch of wavelength and handedness is reversible. The reversible transition of CPL emission wavelength is attributed to the change of emission with temperature. However, the sign reversal of CPL with temperature is due to the change of spin polarization during the transition from self-trapped emission to Mn^{2+} d–d transition emission. The CPL materials with switchable handedness and emission wavelength have great potential applications in information processing and intelligent sensors.

Introduction

Circularly polarized luminescence (CPL) active materials can directly emit left-handed and right-handed circularly polarized light with differences, thus avoiding about 50% light loss. CPL active materials have a wide range of applications in 3D displays, biosensing, encryption and anti-counterfeiting, photocatalytic asymmetric synthesis and other fields.[1–7] Therefore, scientists have been developing CPL active materials with great enthusiasm. Chiral metal halide perovskite has attracted much attention due to its excellent photoelectric properties. Most of the reported CPL-emitting metal halide materials are based on Pb^{2+}. Zang *et al.* synthesized new lead-based perovskite single crystals with chiral *R*-/*S*-cyclohexediamine cations[8] and (*R*-/*S*-2-methylpiperazine)[9] respectively, both of which showed wide band CPL. Luo *et al.* reported a pair of water-resistant 1D hybrid perovskites $(R\text{-}C_5H_{14}N_2)PbBr_4{\cdot}H_2O$ and $(S\text{-}C_5H_{14}N_2)PbBr_4{\cdot}H_2O$, showing opposite yellow–white broadband CPL.[10] Wei's group reported a 0D chiral metal halide $(RR\text{-}/SS\text{-}C_6N_2H_{16})_2Pb_{0.968}Sn_{0.032}Br_6{\cdot}2H_2O$ with both strong CPL and high photoluminescence quantum yield (PLQY).[11] However, the toxicity of Pb^{2+} limits the application of these materials. Therefore, the development of non-toxic and efficient luminous metal halide materials is a key problem to be solved. Organic–inorganic hybrid metal halides based on manganese(II) have become the focus of many researchers.

A large luminescent asymmetric *g* factor (g_{lum}) and high PLQY are important for the technical application of high-performance CPL materials. Many Mn-based metal halides show a high PLQY. Zheng *et al.* reported the organic–inorganic enantiomorphic perovskite (*R*-/*S*)-3-(fluoropyrrolidinium))-$MnBr_3$, which is the first ferroelectric molecule with CPL activity.[12] Zhao's group reported that a pair of environmentally friendly lead-free chiral Mn-based metal halides $(R\text{-}/S\text{-1-MPA})_2MnBr_4$ exhibit CPL properties at room temperature.[13] Gao *et al.* introduced chiral MBA into the manganese bromide

[a] Tianjin Key Laboratory of Applied Catalysis Science and Technology, School of Chemical Engineering and Technology, Tianjin University, No. 135, Yaguan Road, Tianjin 300350, P. R. China. E-mail: shuangjiang@tju.edu.cn
[b] Guangdong Laboratory of Chemistry and Fine Chemical Industry Jieyang Center, Jieyang, 522000, China
[c] CAS Key Laboratory of Standardization and Measurement for Nanotechnology, CAS Center for Excellence in Nanoscience, National Center for Nanoscience and Technology, No. 11 ZhongguancunBeiyitiao, Beijing 100190, China

† Electronic supplementary information (ESI) available. CCDC 2225347 and 2225348. For ESI and crystallographic data in CIF or other electronic format see DOI: https://doi.org/10.1039/d2tc05349g

‡ These authors contributed equally to this work.

framework to prepare (*R*-/*S*-MBA)$_2$MnBr$_4$ and (rac-MBA)[Mn$_2$Br$_5$(EtOH)], respectively, showing significantly different fluorescence emission.[14] Mao *et al.* successfully synthesized four chiral hybrid manganese bromide materials by using different chiral ammonium alkoxide cations.[15] Chiral Mn-based functional materials with CPL have attracted increasing attention due to their excellent luminescence properties and extensive application potential in LED devices.[13] However, current research only focuses on fixed CPL properties, and it is challenging to realize the control of the handedness and color of CPL light. CPL materials with switchable handedness or emission wavelengths play an important role in reducing the need for repeated bottom-up synthesis.

In this study, we introduced (*R*)-(+)-4-bromo-alpha-phenylethylamine (*R*-Br-MBA) and (*S*)-(−)-4-bromo-alpha-phenylethylamine (*S*-Br-MBA) into the manganese bromide framework to synthesize (*R*-/*S*-Br-MBA)$_3$MnBr$_5$ single crystals. The single crystal has a zero-dimensional structure, containing the isolated $[MnBr_4]^{2-}$ tetrahedron surrounded by chiral cations, and heating does not change the crystal structure. Due to the excellent chirality and tunable emission properties of the material, the (*R*-/*S*-Br-MBA)$_3$MnBr$_5$ single crystal realized the reversible conversion of CPL handedness and color, which is temperature-dependent. At room temperature, it shows orange CPL at 634 nm. With the increase of temperature, the CPL displayed by single crystals gradually turns into green at 520 nm with the conversion of the CPL signal. The reversible transition of CPL emission wavelength is attributed to the change of emission properties with temperature. At room temperature, the single crystal shows two emission peaks at 520 nm and 634 nm, attributed to the d–d transition of Mn^{2+} and self-trapping exciton, respectively. The temperature-dependent emission color variation is attributed to the thermally induced trapping and detrapping processes of the self-trapping exciton. The sign reversal of CPL occurs with the increase of temperature because the polarization state of light changes during the transition from self-trapped light to Mn^{2+} d–d transition emission, that is, the spin polarization changes.

Results and discussion

The organic–inorganic hybrid chiral Mn-based metal halides (*R*-/*S*-Br-MBA)$_3$MnBr$_5$ single crystal was prepared from the HBr aqueous solution of *R*-/*S*-Br-MBA and MnBr$_2$ with a molar ratio of 2 : 1 by a slow evaporation method, as shown in Fig. 1a. The newly generated crystals under daylight and ultraviolet lamp are shown in Fig. S1 (ESI†). The single crystals appear as light green under natural light and emit orange fluorescence under 365 nm excitation, which gradually changes to bright green fluorescence after heating. In order to understand the crystal structure of (*R*-Br-MBA)$_3$MnBr$_5$, single crystal X-ray diffraction (SCXRD) tests were performed at room-temperature. In the compound, each Mn atom is surrounded by four Br atoms, resulting in the formation of a separate $[MnBr_4]^{2-}$ tetrahedral unit (Fig. 1b). The surrounding space of $[MnBr_4]^{2-}$ is filled with *R*-Br-MBA$^+$ cations, forming a unique 0D structure, which is similar to that previously reported.[13,14] Each (*R*-Br-MBA)$_3$MnBr$_5$

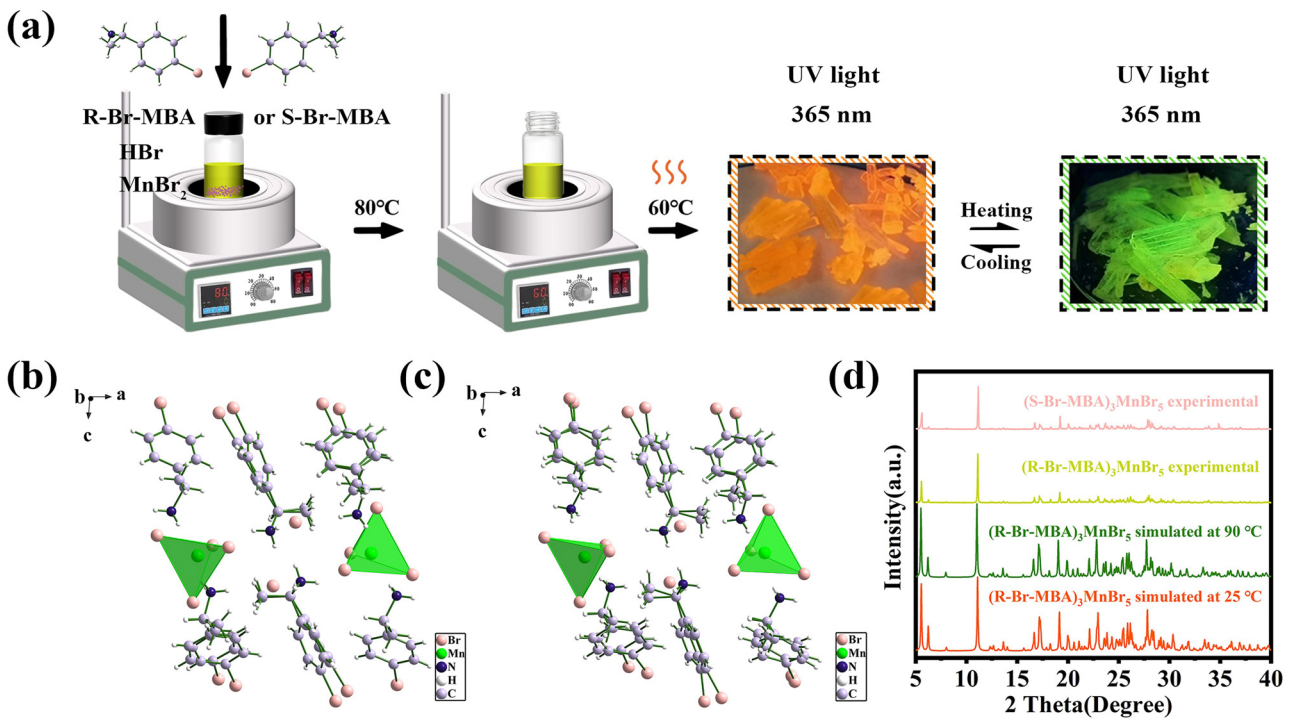

Fig. 1 (a) Schematic diagram of synthesis. The crystal structure of (*R*-Br-MBA)$_3$MnBr$_5$ at (b) 25 °C and (c) 90 °C; (d) PXRD patterns and simulated XRD patterns of (*R*-/*S*-Br-MBA)$_3$MnBr$_5$.

molecule consists of three *R*-Br-MBA$^+$ cations, one $[MnBr_4]^{2-}$ tetrahedron, and one isolated Br^- anion. In particular, two of the three chiral amines coordinated with the tetrahedron appear disordered. Four amines in Fig. 1b look like four pairs of overlapped amines, which are actually disordered. The Mn–Br has a distance range of 2.4848(14) Å to 2.5189(15) Å, and the Br–Mn–Br has an angle range of 103.90(5)° to 114.20(5)°, slightly distorted compared to the ideal tetrahedron's 109.47°. The crystal structure of (*R*-Br-MBA)$_3$MnBr$_5$ is composed of a monocline crystal system and *P*1 2$_1$ 1 spatial groups. The lattice parameters are *a* = 14.2298(1) Å, *b* = 8.0337(1) Å, and *c* = 15.9969(2) Å. The relevant crystal structure parameters are listed in Tables S1–S3 (ESI†).

The crystal structure at 90 °C is the same as that at 25 °C (Fig. 1c). However, crystallographic data (Table S1, ESI†) show that the increase of temperature induces lattice expansion and density reduction. It is speculated that when the heating temperature is below 300 °C, the lattice expansion and structural changes are mainly due to the heat-induced ion vibration in the sublattice, which is mostly a recoverable process.[16,17] During the SCXRD characterization at 90 °C, the high temperature causes all three chiral amines coordinating with $[MnBr_4]^{2-}$ tetrahedron to become disordered, which results in a sudden change in bond length and a partially disordered configuration. According to the crystallographic data (Table S2, ESI†), we find that the length of the Br1–Mn1 bond is shortened from 2.5189 to 2.4835 Å and that of the Br4–Mn1 bond is extended from 2.4848 to 2.5076 Å, the bond lengths of Br2–Mn1 and Br3–Mn changed little. The lattice parameters are *a* = 14.3055(3) Å, *b* = 8.0469(2) Å, *c* = 16.0940(3) Å. The angle between two adjacent Br^- and Mn^{2+} (Br–Mn–Br) ranges from 103.99(6) ° to 114.03(6) °, and the bond spacing between the two Br^- and Mn^{2+} varies from 2.4835(17) Å to 2.5171(18) Å. The measured powder X-ray diffraction (PXRD) diagram of (*R*-Br-MBA)$_3$MnBr$_5$ polycrystalline powder is consistent with the corresponding simulated single crystal data (Fig. 1d), which proves that the purity and homogeneity of the synthesized crystal are good. It can be seen from the simulated XRD patterns (Fig. 1d) that there is no obvious difference between the XRD spectra at 25 °C and the XRD spectra at 90 °C. Therefore, we can confirm that there is no structural transformation after heating. PXRD patterns show that the diffraction peaks of the original and recovered samples are similar (Fig. S2, ESI†), proving that the reversible process does not affect the crystal structure.

To demonstrate the chiral properties of the Mn-based metal halides (*R*-/*S*-Br-MBA)$_3$MnBr$_5$, the circular dichroism (CD) spectra of the crystal were tested in KBr matrix. Fig. 2a and b (top) show CD spectra at 25 °C and 90 °C respectively. (*R*/*S*-Br-MBA)$_3$MnBr$_5$ has an obvious CD signal in the range of 200–300 nm, which are mirror symmetric. The CD spectra at 25 °C and 90 °C show no obvious difference. The CD symbol of (*R*-/*S*-Br-MBA)$_3$MnBr$_5$ changes near the exciton absorption edge, which is a Cotton effect. It is worth noting that, unlike most Pb-based organic–inorganic hybrid perovskites, the absorption and CD signal of the (*R*-/*S*-Br-MBA)$_3$MnBr$_5$ single crystal appear before 300 nm, which is similar to the extinction spectrum of

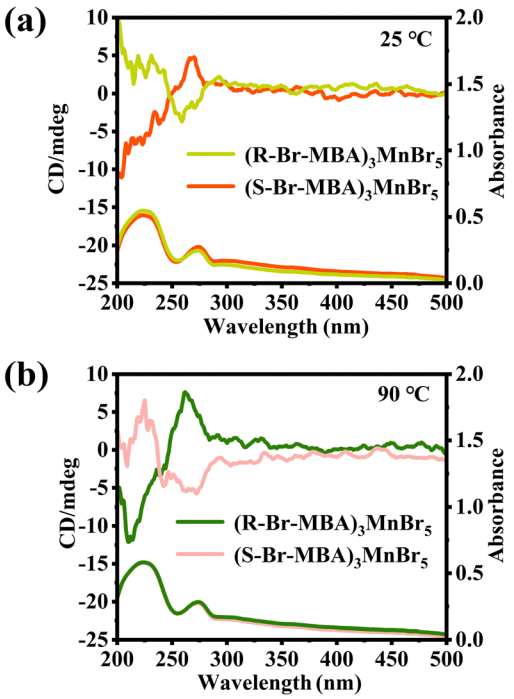

Fig. 2 The CD spectra of (*R*-/*S*-Br-MBA)$_3$MnBr$_5$ at (a) 25 °C and (b) 90 °C.

similar crystal structures.[14] The CD spectra (Fig. S3, ESI†) of the chiral ammonium salt (*R*-/*S*-Br-MBA)Br have been conducted, which is obviously different from that of (*R*-/*S*-Br-MBA)$_3$MnBr$_5$, indicating that the chirality of *R*-/*S*-Br-MBA has been successfully imparted to the whole crystal.

The thermogravimetric (TG) and derivative thermogravimetric (DTG) curves show that for (*R*-Br-MBA)$_3$MnBr$_5$ (Fig. 3a), the first decomposition interval appears at 214–300 °C, and the second decomposition interval appears at 300–328 °C with the continuous increase of temperature, which corresponds to the decomposition of an organic ammonium salt and some carbides. The third decomposition interval ranges from 512 to 774 °C, and the peak of the weight change rate curve is 715 °C, corresponding to the continuous decomposition of carbides and the beginning of the melting or decomposition of $MnBr_2$ (with the melting point of 698 °C). The temperature continues to rise until the test is over and the weight no longer changes. The TG and DTG curves of (*S*-Br-MBA)$_3$MnBr$_5$ are similar to those of (*R*-Br-MBA)$_3$MnBr$_5$ (Fig. S4, ESI†).

The TG and DTG curves show that the initial weight loss temperature of (*R*-Br-MBA)$_3$MnBr$_5$ is up to 214 °C, which fully highlights its thermal stability. Next, Fourier transform infrared spectroscopy (FTIR) of the (*R*-/*S*-Br-MBA)$_3$MnBr$_5$ crystal was measured at 25 °C and 90 °C, respectively (Fig. 3b and Fig. S5, ESI†). The strong peak at 1570, 1518 and 823 cm^{-1} is the characteristic peak of the benzene ring, the wide peak at 3250–2850 cm^{-1} is the stretching vibration peak of the protonated amino group, and the wide absorption in the range of 3000–3600 cm^{-1} is attributed to the H–O stretching vibration of bound water (υ_{H-O}). Mn-based metal halides are generally hygroscopic and absorb a small number of water molecules

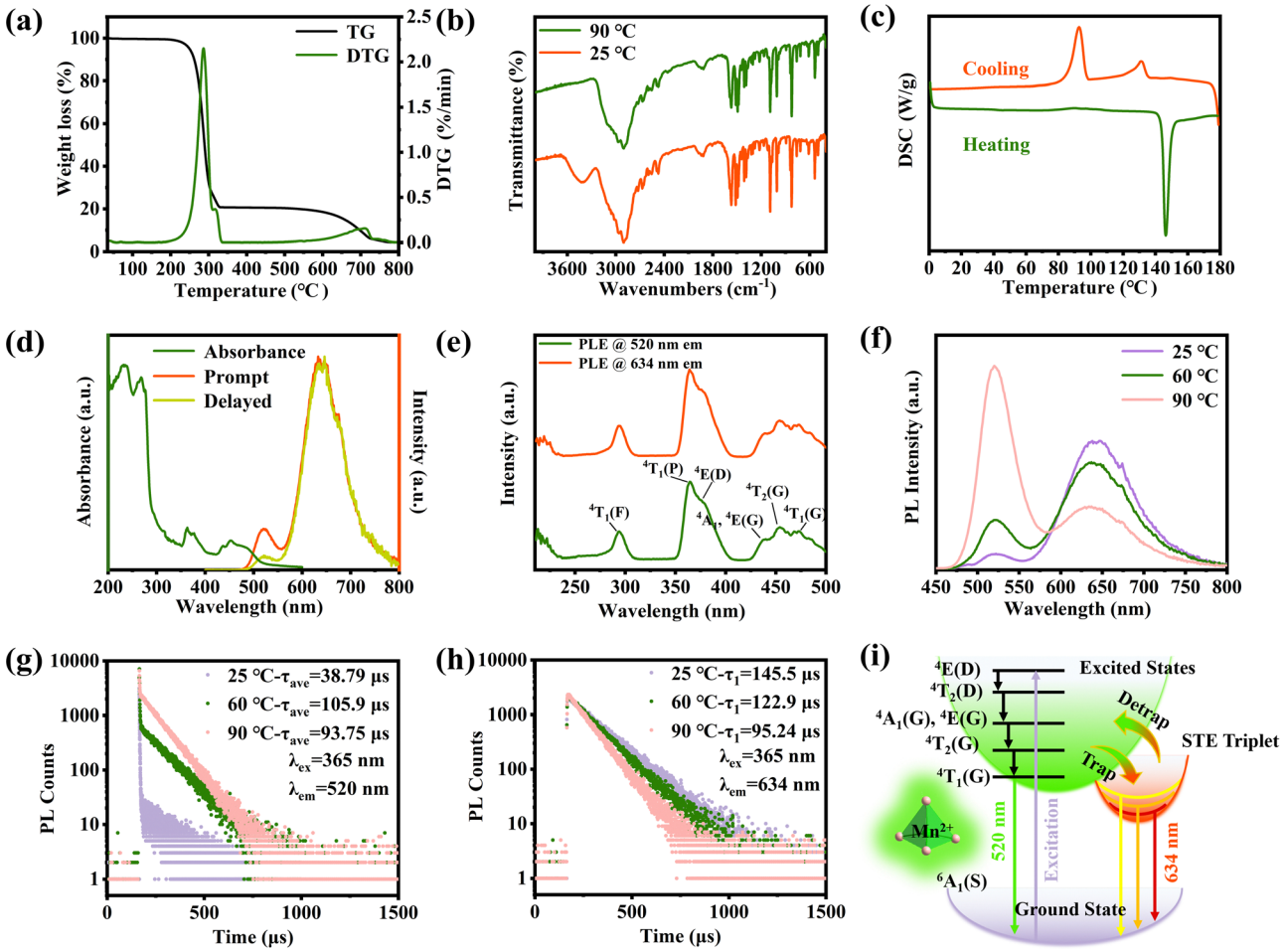

Fig. 3 (a) TG and DTG curves of $(R\text{-Br-MBA})_3MnBr_5$; (b) the FTIR spectra of $(R\text{-Br-MBA})_3MnBr_5$ at 25 °C and 90 °C; (c) DSC curve of $(R\text{-Br-MBA})_3MnBr_5$ single crystal in the temperature range of 0–180 °C; (d) absorption, prompt PL, and delayed PL spectra of $(R\text{-Br-MBA})_3MnBr_5$; (e) PLE spectra of $(R\text{-Br-MBA})_3MnBr_5$ with emission wavelengths at 520 nm and 634 nm; (f) temperature-dependent PL spectra of $(R\text{-Br-MBA})_3MnBr_5$; (g) time-resolved PL spectra of 520 nm at 25 °C, 60 °C and 90 °C, respectively; (h) time-resolved PL spectra of 634 nm at 25 °C, 60 °C and 90 °C, respectively; (i) temperature-sensitive PL decay mechanism in $(R\text{-}/S\text{-Br-MBA})_3MnBr_5$.

in the air. The FTIR of the crystals tested at 90 °C show that the peak disappears at 3428 cm^{-1}, because adsorbed water molecules can usually be slightly removed by heating. Then we conducted differential scanning calorimeter (DSC) tests in the temperature range of 0–180 °C as shown in Fig. 3c. The curve shows that $(R\text{-Br-MBA})_3MnBr_5$ exhibits a typical first-order phase transition at 146 °C. The emission color changes from orange to green with the increase in temperature (25–90 °C), but no phase transition is observed in the temperature range. Therefore, the thermoresponsive emission variation can rule out a phase transition.[18,19]

To further characterize the optical properties of $(R\text{-}/S\text{-Br-MBA})_3MnBr_5$, we measured its absorption spectrum at room temperature (Fig. 3d). There are five main absorption bands in the range of 200–800 nm, concentrated at 234, 268, 365 and 451 nm. The absorption bands at 234 nm and 268 nm are derived from the amino and phenyl groups of *R*-Br-MBA, respectively, and the two peaks at 365 nm and 451 nm can be attributed to the electronic transition from the $^6A_1$ ground state of Mn^{2+} with d-electron configuration to the different excited states of $[MnBr_4]^{2-}$, such as $[^4A_1(G), {}^4E(G)]$ (439 nm) and $^4T_1(G)$ energy level (472 nm).[20,21] Typical absorption is accompanied by tetrahedral crystal field transitions and ligand field splitting, which are similar to transitions in other Mn-based crystal structures.[13,22,23] After turning off the excitation, a PL spectrum with a delay time of 1 ms was recorded for comparison with the prompt PL spectrum (Fig. 3d). The result shows that the fluorescence peak intensity of delayed PL is weakened at 520 nm. In the range of 600–800 nm, the peak of the delayed PL spectrum overlaps perfectly with the prompt PL spectrum, indicating the emission of $(R\text{-}/S\text{-Br-MBA})_3MnBr_5$ feature phosphorescence characteristics.[24] Fig. 3e shows the PL excitation (PLE) spectra of $(R\text{-Br-MBA})_3MnBr_5$ powders at room temperature, and the PLE spectra are consistent with the absorption spectra.

In previous studies, Mn-based metal halides usually have only one emission band, corresponding to red or green emission. In the case of A_2MnX_4, the Mn atom forms a $[MnX_4]^{2-}$ tetrahedral unit with four halide ions. The large distance

between Mn–Mn eliminates the direct spin–spin coupling, and the optical transition is dominated by the independent Mn^{2+} ion. Therefore, it usually shows green emissions.[23,25] In the case of $AMnX_3$, $[MnX_6]^{4-}$ eight sides share to form a linear chain. The Mn–Mn distance is greatly reduced, which significantly affects the d–d transition rule and transition energy so that the octahedral coordination of $AMnX_3$ shows an orange-to-red emission.[14] However, our observations are significantly different from those reported above. A (*R*-/*S*-Br-MBA)$_3MnBr_5$ single crystal displays orange emission at room temperature. With the increase of temperature, the single crystal gradually turns into green emission. From the DSC test results, we have excluded the emission color change caused by phase transition. In addition, the single crystal analysis results of (*R*-Br-MBA)$_3MnBr_5$ show that the crystal structure remain the same at 25 °C and 90 °C, both of which are zero-dimensional tetrahedrons with almost the same crystal parameters (Tables S1–S3, ESI†). Therefore, the emission color transformation does not originate from the change in manganese ion coordination environment. The expansion or contraction of interatomic distance caused by external factors such as temperature and pressure may change the band gap of hybrid perovskite.[26,27] Temperature is known to cause lattice thermal expansion and modify carrier–phonon and phonon–phonon interactions, which may lead to electronic structure renormalization and changes in optical properties,[28,29] resulting in thermochromic phenomenon. However, the position of the absorption peak of (*R*-/*S*-Br-MBA)$_3MnBr_5$ did not change with the increase of temperature (Fig. 2), indicating no change in the band gap. Therefore, we exclude the possibility that lattice expansion causes the color change. Recently, some research shows that the wideband emission of low-dimensional metal halides with large Stokes shifts are attributed to the emission of self-trapping excitons (STEs).[30–33] The as-prepared (*R*-Br-MBA)$_3MnBr_5$ shows large Stokes shifts and similar thermochromic properties.[18,19] So in our case, it is reasonable to attribute the emission peaks at 520 nm and 634 nm of (*R*-/*S*-Br-MBA)$_3MnBr_5$ to the d–d transition of Mn^{2+} and self-agglutination exciton, respectively.

First, excitation wavelength-dependent PL spectra were measured to verify the hypothesis (Fig. S6, ESI†). The normalized PL spectra show little change in the 268–451 nm excitation wavelength, which excludes the possibility of the emission from impurity. Considering that the formation of STEs is a thermal activation process, we expect that temperature may influence the relative PL intensity of the two emissions of the (*R*-Br-MBA)$_3MnBr_5$ single crystal. To test this conjecture, temperature-dependent PL spectra were collected (Fig. 3f). Clearly, there is a competition of PL intensity between the two emissions with varying temperature. As the crystal is gradually heated from 25 °C to 90 °C, the orange emission is gradually weakened and the green emission is enhanced, resulting in a significant reduction of $I_{634\ nm}/I_{520\ nm}$ (Fig. S7, ESI†), resulting in the single crystal emission color changing from orange to green (Fig. 3f). In addition, when the temperature is lowered, both the luminescence spectrum and the emission color recover, which indicates that the heat-induced emission changes have good reversibility.

Subsequently, as shown in Fig. 3g and h, we obtained the PL lifetime of (*R*-Br-MBA)$_3MnBr_5$ at room temperature and 90 °C by using time-resolved photoluminescence (TRPL) spectra with an excitation wavelength of 365 nm. The lifetime of TRPL emitted at 520 nm shows a double exponential attenuation of about 38.79 μs at 25 °C, which significantly increases to 105.9 μs at 60 °C and 93.75 μs at 90 °C. The relatively long fluorescence lifetime verifies that the emission is phosphorescence and it indicates that the spin of Mn^{2+} prohibits the d–d transition.[34] In contrast, the TRPL emitted at 634 nm shows single exponential attenuation of 145.5 μs, 122.9 μs, and 95.24 μs at 25 °C, 60 °C and 90 °C, respectively (Fig. 3h). The long PL lifetime is consistent with the reported values of STE emission in low-dimensional metal halides, indicating that the orange emission at 634 nm may be from a triplet state.[35–37] The fluorescence quantum yield (PLQY) of (*R*-Br-MBA)$_3MnBr_5$ was determined to further evaluate the emission efficiency. The PLQY is 6.47% at room temperature and 4.23% at 90 °C (Fig. S8, ESI†), respectively. It is known that the dipole-dipole interaction at the interface Mn^{2+} center of the $[MnBr_4]^{2-}$ unit is very important. It significantly affects the energy transfer center between Mn^{2+}, and the coupling strength depends on the Mn–Mn distance. The longer average Mn···Mn distance favors a higher PLQY because the energy transfer process between adjacent Mn centers is reduced.[38] For (*R*-Br-MBA)$_3MnBr_5$, the Mn···Mn distance is 6.1477 Å at room temperature and 6.1610 Å at 90 °C, respectively. Due to the compact configuration of the organic cation *R*-Br-MBA, the distance between adjacent manganese ion centers is small both at room temperature and 90 °C. Therefore, there is a stronger dipole–dipole coupling interaction between neighboring $[MnBr_4]^{2-}$ in (*R*-Br-MBA)$_3MnBr_5$.[39] This enhances nonradiative energy transfer between adjacent $[MnBr_4]^{2-}$centers. In addition, in our (*R*-/*S*-Br-MBA)$_3MnBr_5$ structure, there is an isolated Br^- anion in the structure due to the formation of a hydrogen bond with organic cations, and the existence of additional Br^- ions may affect the PLQY.[40] Ultimately, we obtained a low PLQY.

The underlying mechanism of temperature-sensitive PL is shown in Fig. 3i. Under ultraviolet irradiation, the ground state electrons are excited from $^6A_1$ to $^4T_1$, $^4E(G)$, or even higher energy than $^4E(D)$ in the Mn^{2+} d–d orbital.[41] At room temperature, either structural recombination or local excitons of excited states may lead to the formation of triplet STEs.[36] In this way, an efficient broadband phosphorescence emission with a large Stokes shift at 634 nm is produced at room temperature when the exciton relaxes to the ground state. As the temperature increases, STE obtains enough energy to escape the trap state, resulting in the increase of thermal quenching of STE. Therefore, excitons are more easily captured by the $^4T_1(G)$ level of Mn^{2+}, inducing the radiation transition of $^4T_1$–$^6A_1$ Mn^{2+} ions and resulting in phosphorescence emission at 520 nm.[18]

In order to understand the Mn–Mn coupling and ferromagnetism of the sample, a SQUID-VSM magnetic measurement system was used to characterize the magnetic properties of the prepared Mn-based metal halides (*R*-/*S*-Br-MBA)$_3MnBr_5$ single crystal. The magnetic fields of -2T to 2T were uniformly applied

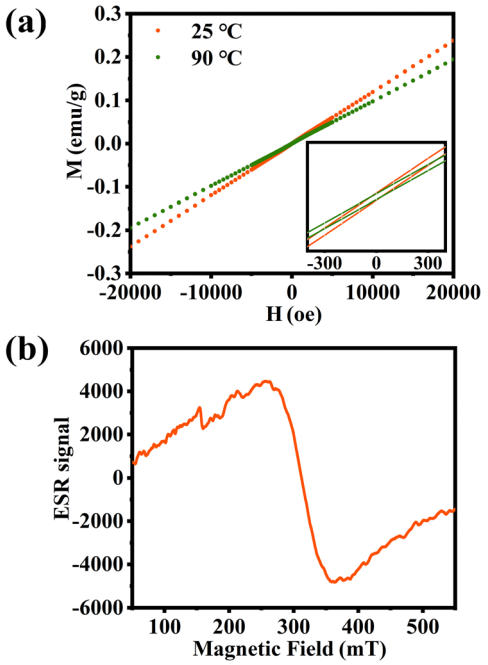

Fig. 4 (a) Hysteresis loops of (*R*-Br-MBA)$_3$MnBr$_5$ crystal at 25 °C and 90 °C; (b) ESR spectra of (*R*-Br-MBA)$_3$MnBr$_5$ single crystal at 25 °C.

to the two samples, and the magnetic hysteresis (M–H) loops of (*R*-/*S*-Br-MBA)$_3$MnBr$_5$ single crystals were measured at 25 °C and 90 °C, respectively. As shown in Fig. 4a and Fig. S9 (ESI†), the hysteresis loops of (*R*-/*S*-Br-MBA)$_3$MnBr$_5$ single crystal at 25 °C and 90 °C show a linear M–H relationship, and the coercivity and remanence are negligible, indicating that (*R*-/*S*-Br-MBA)$_3$MnBr$_5$ is a paramagnetic material at 25 °C and 90 °C. Compared with the hysteresis loops at 25 °C, the magnetic properties at 90 °C are decreased. However, although the M–H loop of (*R*-/*S*-Br-MBA)$_3$MnBr$_5$ is a straight line through the first and third quadrants, the enlarged region near the zero magnetic fields of the M–H loop clearly shows that the M–H loops do not coincide exactly (Fig. 4a, illustration). It indicates that (*R*-/*S*-Br-MBA)$_3$MnBr$_5$ still has weak ferromagnetic coupling species, and the nearest Mn–Mn distance is 6.1477 Å, which is less than the critical distance between the paramagnetic and ferromagnetic phases of Mn ion in Mn-based metal halides (6.6 Å).[42] In addition, X-band ESR spectroscopy was used to study the surrounding environment of Mn^{2+} ions in room-temperature samples, as shown in Fig. 4b. It can be seen that a continuous wide dipole peak replaces the hyperfine splitting mode of a single Mn^{2+} ion, indicating the presence of weak ferromagnetic interaction between adjacent Mn^{2+} in the compound.[43,44] ESR results are consistent with M–H curves, indicating that Mn–Mn pairs or clusters with weak ferromagnetic coupling exist in (*R*-/*S*-Br-MBA)$_3$MnBr$_5$ single crystals. Generally speaking, the increase of temperature will cause lattice expansion, which will further increase the Mn–Mn distance, thus reducing concentration quenching between locally adjacent Mn ions. According to the single crystal structure, the minimum Mn–Mn distance increases from 6.1477 Å at 25 °C to 6.1610 Å at 90 °C, which is consistent with the variation trend of the hysteresis loop.

Since the synthesized Mn-based metal halides have unique emission reversible transformation characteristics and chiral signals, the CPL dynamic switching property has been investigated. The CPL spectra of (*R*-/*S*-Br-MBA)$_3$MnBr$_5$ powder were recorded at 0 °C, 25 °C, 60 °C and 90 °C respectively (Fig. 5). The emission of CPL further indicates that the chirality of chiral organic cations has been successfully introduced into the entire (*R*-/*S*-Br-MBA)$_3$MnBr$_5$ crystal. As shown in Fig. 5, for (*R*-Br-MBA)$_3$MnBr$_5$ (Fig. 5, solid line), the sample shows orange CPL emission at 634 nm at 0 °C and 25 °C, and the CPL sign is positive ((+)-CPL). When the temperature increases to 60 °C, the CPL signal transforms to green CPL emission at 520 nm, and the CPL sign is negative ((−)-CPL). When the temperature rises to 90 °C, it completely transforms into green CPL emission at 520 nm. That is, the increase of temperature induces the blue shift of CPL emission wavelength (from 634 nm to 520 nm) and the flip of CPL signal (from (+)-CPL to (−)-CPL). For (*S*-Br-MBA)$_3$MnBr$_5$ (Fig. 5, dashed line), the sample exhibits orange negative (−)-CPL emission at 634 nm at 0 °C and 25 °C. When the temperature increases to 60 °C, it transforms into green

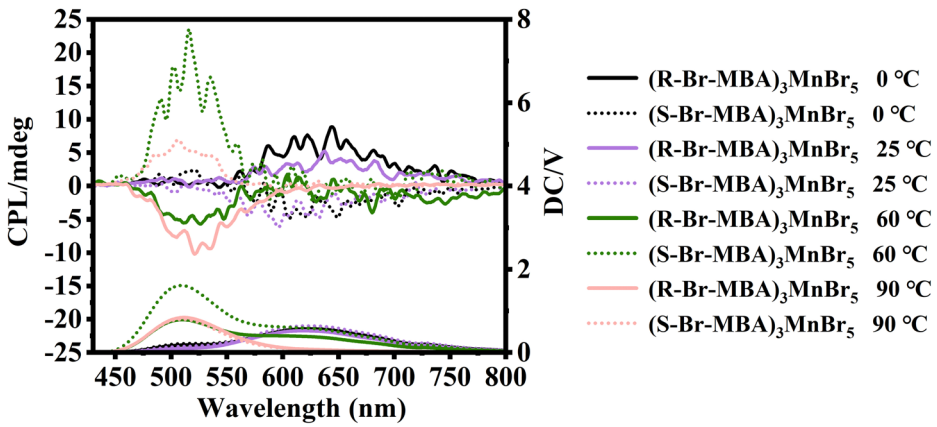

Fig. 5 The CPL spectra of (*R*-/*S*-Br-MBA)$_3$MnBr$_5$ powder at 0 °C, 25 °C, 60 °C and 90 °C.

CPL emission with positive (+)-CPL at 520 nm. When the temperature rises to 90 °C, it completely transforms into green CPL emission at 520 nm with positive (+)-CPL. Therefore, variable emission color and CPL switching in +/− are achieved in the prepared chiral manganese halides.

$$g_{\mathrm{lum}} = \frac{\mathrm{CPL\ [mdeg]} \times \ln 10}{32\,980 \times \mathrm{DC\ (V)}} \quad (1)$$

The luminescent asymmetrical g factor (g_{lum}) is an important parameter for quantifying CPL emission. The g_{lum} of chiral Mn-based metal halide was calculated using eqn (1) (Fig. S10, ESI†). At 0 °C, the g_{lum} of (*R*-Br-MBA)$_3$MnBr$_5$ and (*S*-Br-MBA)$_3$MnBr$_5$ at 634 nm are 9.1×10^{-4} and -4.8×10^{-4}, respectively. When the temperature is 25 °C, the g_{lum} of (*R*-Br-MBA)$_3$MnBr$_5$ and (*S*-Br-MBA)$_3$MnBr$_5$ at 634 nm is 3.6×10^{-4} and -4.2×10^{-4}, respectively. At 60 °C, the g_{lum} of (*R*-Br-MBA)$_3$MnBr$_5$ and (*S*-Br-MBA)$_3$MnBr$_5$ at 520 nm is -5.2×10^{-4} and 7.1×10^{-4}, respectively. When the temperature is 90 °C, the g_{lum} of (*R*-Br-MBA)$_3$MnBr$_5$ and (*S*-Br-MBA)$_3$MnBr$_5$ at 520 nm is -5.8×10^{-4} and 5.6×10^{-4}, respectively. The (*R*-/*S*-Br-MBA)$_3$MnBr$_5$ single crystal at room temperature has dual emission, which originates from the radiative recombination of Mn^{2+} d–d orbital transition and STE. The competition between the two radiation paths produced a significant and reversible transition of CPL emission wavelength in (*R*-/*S*-Br-MBA)$_3$MnBr$_5$ single crystal. The CPL spectrum has a sign reversal with the increase in temperature, but the CD spectrum does not change significantly with the increase in temperature. With the increase of temperature, the polarization state of light changes during the transition from self-trapped light to Mn^{2+} d–d transition phosphorescence, that is, the spin polarization changes during the transition from excited state to ground state. Therefore, the CPL spectrum has sign reversal with the increase of temperature. The chirality of the electron transition from the ground state to the excited state does not change with temperature. Thus, the CD signal has no obvious change.

Conclusions

In conclusion, we successfully synthesized a pair of environmentally friendly chiral Mn-based metal halides (*R*-/*S*-Br-MBA)$_3$MnBr$_5$ with CPL activity. The chiral crystals realize intelligent regulation of CPL property, with the simultaneous regulation of color and direction of polarization. (*R*-/*S*-Br-MBA)$_3$MnBr$_5$ display orange CPL at room temperature and turn to green CPL with the increase of temperature, along with the reversal of the CPL direction. The transition of CPL emission wavelength is attributed to the temperature-dependent phosphorescence behaviour, which comes from two competitive radiation paths: the radiative recombination of the Mn^{2+} d–d orbital transition and STE emission. The temperature-dependent emission color variation is attributed to the thermally induced trapping and detrapping processes of the self-trapping exciton. The sign reversal of CPL occurs because the polarization state of light changes during the transition from self-trapped light to Mn^{2+} d–d transition phosphorescence, that is, the spin polarization changes. Our results show that the material can be used for reversible conversion of CPL handedness and color, which opens up new possibilities for improving the function of the material.

Conflicts of interest

The authors declare no competing financial interest.

Acknowledgements

This work was financially supported by the National Natural Science Foundation of China (22278315), and the Tianjin Municipal Natural Science Foundation (21JCQNJC00610).

Notes and references

1 Y. T. Sang, J. L. Han, T. H. Zhao, P. F. Duan and M. H. Liu, *Adv. Mater.*, 2020, **32**, 1900110.
2 Y. Z. Dong, Y. P. Zhang, X. Y. Li, Y. Q. Feng, H. Zhang and J. L. Xu, *Small*, 2019, **15**, 1902237.
3 G. K. Long, R. Sabatini, M. I. Saidaminov, G. Lakhwani, A. Rasmita, X. G. Liu, E. H. Sargent and W. B. Gao, *Nat. Rev. Mater.*, 2020, **5**, 423–439.
4 D. X. Han, C. X. Li, C. Y. Jiang, X. Jin, X. B. Wang, R. Chen, J. J. Cheng and P. F. Duan, *Aggregate*, 2022, **3**, e148.
5 Y. Gao, C. Ren, X. D. Lin and T. C. He, *Front. Chem.*, 2020, **8**, 458.
6 Z. L. Gong, X. F. Zhu, Z. H. Zhou, S. W. Zhang, D. Yang, B. Zhao, Y. P. Zhang, J. P. Deng, Y. X. Cheng, Y. X. Zheng, S. Q. Zang, H. Kuang, P. F. Duan, M. J. Yuan, C. F. Chen, Y. S. Zhao, Y. W. Zhong, B. Z. Tang and M. H. Liu, *Sci. China: Chem.*, 2021, **64**, 2060–2104.
7 F. M. Xie, J. X. Zhou, X. Y. Zeng, Z. D. An, Y. Q. Li, D. X. Han, P. F. Duan, Z. G. Wu, Y. X. Zheng and J. X. Tang, *Adv. Opt. Mater.*, 2021, **9**, 2100017.
8 X. H. Zhao, X. Z. Hu, M. E. Sun, X. M. Luo, C. Zhang, G. S. Chen, X. Y. Dong and S. Q. Zang, *J. Mater. Chem. C*, 2022, **10**, 3440–3446.
9 K. H. Jin, Y. Zhang, K. J. Li, M. E. Sun, X. Y. Dong, Q. L. Wang and S. Q. Zang, *Angew. Chem., Int. Ed.*, 2022, **61**, e202205317.
10 Y. Peng, X. Wang, L. N. Li, H. Ye, S. Yang, H. G. Yang, J. H. Luo and Y. Hou, *Adv. Opt. Mater.*, 2022, 2201888.
11 Y. Wei, C. Li, Y. W. Li, Z. S. Luo, X. Y. Wu, Y. L. Liu, L. M. Zhang, X. He, W. Wang and Z. W. Quan, *Angew. Chem., Int. Ed.*, 2022, e202212685.
12 J. X. Gao, W. Y. Zhang, Z. G. Wu, Y. X. Zheng and D. W. Fu, *J. Am. Chem. Soc.*, 2020, **142**, 4756–4761.
13 B. B. Wang, C. Wang, Y. Chu, H. Y. Zhang, M. J. Sun, H. Wang, S. P. Wang and G. J. Zhao, *J. Alloys Compd.*, 2022, **910**, 164892.
14 W. D. Cai, J. J. Qin, T. Q. Pang, X. Y. Cai, R. X. Jia and F. Gao, *Adv. Opt. Mater.*, 2022, 2102140.

15 J. Chen, S. Zhang, X. Pan, R. Q. Li, S. Ye, A. K. Cheetham and L. L. Mao, *Angew. Chem., Int. Ed.*, 2022, **134**, e202205906.
16 Y. R. Zhang, Y. L. Song, Y. Lu, Z. Zhang, Y. Wang, Y. Yang, Q. F. Dong, Y. Yu, P. Qin and F. Q. Huang, *Small*, 2022, **18**, 2201943.
17 W. Ning, X. G. Zhao, J. Klarbring, S. Bai, F. Ji, F. Wang, S. I. Simak, Y. Tao, X. M. Ren, L. Zhang, W. Huang, I. A. Abrikosov and F. Gao, *Adv. Funct. Mater.*, 2019, **29**, 1807375.
18 X. M. Jiang, S. Q. Xia, J. Zhang, D. X. Ju, Y. Liu, X. B. Hu, L. Wang, Z. L. Chen and X. T. Tao, *ChemSusChem*, 2019, **12**, 5228–5232.
19 H. Peng, T. Huang, B. S. Zou, Y. Tian, X. X. Wang, Y. C. Guo, T. T. Dong, Z. M. Yu, C. J. Ding, F. Yang and J. P. Wang, *Nano Energy*, 2021, **87**, 106166.
20 X. M. Jiang, Z. L. Chen and X. T. Tao, *Front. Chem.*, 2020, **8**, 352.
21 J. Chen, Q. Zhang, F. K. Zheng, Z. F. Liu, S. H. Wang, A. Q. Wu and G. C. Guo, *Dalton Trans.*, 2015, **44**, 3289–3294.
22 X. Bai, H. Zhong, B. Chen, C. Chen, J. Han, R. Zeng and B. Zou, *J. Phys. Chem. C*, 2018, **122**, 3130–3137.
23 W. R. Gao, M. Y. Leng, Z. X. Hu, J. Z. Li, D. H. Li, H. Liu, L. Gao, G. D. Niu and J. Tang, *Dalton Trans.*, 2020, **49**, 5662–5668.
24 S. Y. Liu, X. Y. Fang, B. Lu and D. P. Yan, *Nat. Commun.*, 2020, **11**, 4649.
25 X. M. Jiang, Z. L. Chen and X. T. Tao, *Front. Chem.*, 2020, **8**, 352.
26 L. Wu, Z. Dong, L. Zhang, C. Liu, K. Wang and B. Zou, *ChemSusChem*, 2019, **12**, 3971.
27 A. M. Goforth, M. A. Tershansy, M. D. Smith, L. Peterson, J. G. Kelley, W. J. I. Debenedetti and H.-C. Z. Loye, *J. Am. Chem. Soc.*, 2011, **133**, 603.
28 W. A. Saidi and A. Kachmar, *J. Phys. Chem. Lett.*, 2018, **9**, 7090–7097.
29 A. Singh and S. Satapathi, *Adv. Opt. Mater.*, 2021, **9**, 2101062.
30 Y. L. Liu, C. Wang, Y. R. Guo, L. L. Ma, C. Y. Zhou, Y. Liu, L. N. Zhu, X. Z. Li, M. X. Zhang and G. J. Zhao, *J. Mater. Chem. C*, 2020, **8**, 5673–5680.
31 L. Zhou, J. F. Liao, Z. G. Huang, J. H. Wei, X. D. Wang, H. Y. Chen and D. B. Kuang, *Angew. Chem., Int. Ed.*, 2019, **131**, 15581–15586.
32 J. C. Yu, J. T. Kong, W. Hao, X. T. Guo, H. J. He, W. R. Leow, Z. Y. Liu, P. Q. Cai, G. D. Qian, S. Z. Li, X. Y. Chen and X. D. Chen, *Adv. Mater.*, 2019, **31**, 1806385.
33 C. K. Deng, G. J. Zhou, D. Chen, J. Zhao, Y. G. Wang and Q. L. Liu, *J. Phys. Chem. Lett.*, 2020, **11**, 2934–2940.
34 J. Zhao, T. J. Zhang, X. Y. Dong, M. E. Sun, C. Zhang, X. L. Li, Y. S. Zhao and S. Q. Zang, *J. Am. Chem. Soc.*, 2019, **141**, 15755–15760.
35 C. K. Zhou, Y. Tian, Z. Yuan, H. R. Lin, B. H. Chen, R. Clark, T. Dilbeck, Y. Zhou, J. Hurley, J. Neu, T. Besara, T. Siegrist, P. Djurovich and B. W. Ma, *ACS Appl. Mater. Interfaces*, 2017, **9**, 44579–44583.
36 C. K. Zhou, H. R. Lin, Y. Tian, Z. Yuan, R. Clark, B. H. Chen, L. J. van de Burgt, J. C. Wang, Y. Zhou, K. Hanson, Q. J. Meisner, J. Neu, T. Besara, T. Siegrist, E. Lambers, P. Djurovich and B. W. Ma, *Chem. Sci.*, 2018, **9**, 586–593.
37 P. F. Fu, M. L. Huang, Y. Q. Shang, N. Yu, H. L. Zhou, Y. B. Zhang, S. Y. Chen, J. K. Gong and Z. J. Ning, *ACS Appl. Mater. Interfaces*, 2018, **10**, 34363–34369.
38 L. L. Mao, P. J. Guo, S. X. Wang, A. K. Cheetham and R. Seshadri, *J. Am. Chem. Soc.*, 2020, **142**, 13582–13589.
39 H. M. Pan, Q. L. Yang, X. X. Xing, J. P. Li, F. L. Meng, X. Zhang, P. C. Xiao, C. Y. Yue and X. W. Lei, *Chem. Commun.*, 2021, **57**, 6907–6910.
40 L. L. Mao, P. J. Guo, S. X. Wang, A. K. Cheetham and R. Seshadri, *J. Am. Chem. Soc.*, 2020, **142**, 13582–13589.
41 P. Tao, S. J. Liu and W. Y. Wong, *Adv. Opt. Mater.*, 2020, **8**, 2000985.
42 T. Huang, H. Peng, Q. L. Wei, C. Y. Peng, Y. Tian, S. F. Yao, X. X. Han and B. S. Zou, *Nano Energy*, 2022, **93**, 106863.
43 Z. J. Li, E. Hofman, A. H. Davis, A. Khammang, J. T. Wright, B. Dzikovski, R. W. Meulenberg and W. W. Zheng, *Chem. Mater.*, 2018, **30**, 6400–6409.
44 G. J. Zhou, X. X. Jiang, M. Molokeev, Z. S. Lin, J. Zhao, J. Wang and Z. G. Xia, *Chem. Mater.*, 2019, **31**, 5788–5795.

